

# Hydration mechanisms of scheelite from adsorption isotherms and ab initio molecular dynamics simulations

Y. Foucaud, R.L.S. Canevesi, A. Celzard, Vanessa Fierro, M. Badawi

▶ **To cite this version:**

Y. Foucaud, R.L.S. Canevesi, A. Celzard, Vanessa Fierro, M. Badawi. Hydration mechanisms of scheelite from adsorption isotherms and ab initio molecular dynamics simulations. Applied Surface Science, 2021, 562, pp.150137. 10.1016/j.apsusc.2021.150137 . hal-03381716

**HAL Id: hal-03381716**

**https://hal.univ-lorraine.fr/hal-03381716**

Submitted on 17 Oct 2021

**HAL** is a multi-disciplinary open access archive for the deposit and dissemination of scientific research documents, whether they are published or not. The documents may come from teaching and research institutions in France or abroad, or from public or private research centers.

L'archive ouverte pluridisciplinaire **HAL**, est destinée au dépôt et à la diffusion de documents scientifiques de niveau recherche, publiés ou non, émanant des établissements d'enseignement et de recherche français ou étrangers, des laboratoires publics ou privés.



Distributed under a Creative Commons Attribution - NonCommercial - NoDerivatives 4.0 International License

# Hydration mechanisms of scheelite from adsorption isotherms and *ab initio* molecular dynamics simulations

Y. Foucaud,[1,*] R.L.S. Canevesi,[2] A. Celzard,[2] V. Fierro,[2,*] M. Badawi[3,*]

[1]Université de Lorraine, CNRS, GeoRessources, F-54000 Nancy, France.

[2]Université de Lorraine, CNRS, IJL, F-88000 Epinal, France

[3]Université de Lorraine, CNRS, LPCT, F-54000 Nancy, France

**Corresponding Authors**

E-mail: yann.foucaud@univ-lorraine.fr, vanessa.fierro@univ-lorraine.fr, michael.badawi@univ-lorraine.fr

**Abstract**

Apart from its interesting optical properties, scheelite is one of the main tungsten-bearing minerals, widely processed by the froth flotation method. A precise and comprehensive description of the hydration state of scheelite is required to achieve satisfactory flotation performance. The hydration mechanisms of scheelite have been poorly studied, using only theoretical methods. Manometric gas sorption experiments were combined with *ab initio* molecular dynamics simulations, including correction for dispersive interactions. The isosteric enthalpy of adsorption was used as the value to link experimental and theoretical results, since it can be determined by both methods. We have found that water adsorbs more favorably in its molecular form, with two adsorbed water molecules per calcium atom on the (001) surface,

and with three adsorbed water molecules for two calcium atoms on the (112) surface. The very first water molecules adsorb with an isosteric enthalpy of adsorption of -80 kJ·mol$^{-1}$ on the (001) surface, and of -117 kJ·mol$^{-1}$ on the (112) surface, at 300 K. This is in very good agreement with the value of -90 kJ·mol$^{-1}$ calculated using the Clausius-Clapeyron approach on three experimental isotherms, accurately fitted with a dual-site Freundlich-Langmuir model.

**Keywords:** Manometric gas sorption, *Ab initio* molecular dynamics, Dual-site Freundlich-Langmuir, Adsorption, Coverage

**Highlights:**

- Water adsorbs in molecular form on scheelite rather than in dissociated form
- The enthalpy of adsorption of a single molecule on the (112) surface is -117 kJ·mol$^{-1}$
- The enthalpy of adsorption of a single molecule on the (001) surface is -80 kJ·mol$^{-1}$
- The experimental enthalpy of adsorption value is around -90 kJ·mol$^{-1}$ at low coverage
- The high adsorption enthalpies unravel the poor floatability of scheelite

## 1. Introduction

Scheelite ($CaWO_4$), as part of the tungstate family, displays interesting structural [1,2] and luminescence properties [3–6]. It is therefore used in a wide range of industrial applications, including catalysts [7–10], lasers [3,11–13], scintillators [14–16], MASER materials [17–19] and lubricants [20]. Besides, scheelite is one of the main minerals exploited for the extraction of tungsten [21–25], which is widely used in alloys and supra-alloys [26]. Over the past decade, the risk of tungsten supply shortages in Western countries has significantly increased, which, considering the high economic importance of tungsten, led to its classification as a critical raw material in the European Union [27] and in the USA [28]. Scheelite is mainly encountered in skarn deposits that currently represent more than 40% of the tungsten global reserves [21–23]. In skarns, scheelite is commonly associated with other semi-soluble minerals, such as apatite, calcite, and fluorite, from which its separation is required [25,29,30]. Although gravity separation is a common and efficient route for scheelite concentration [31,32], the increasing demand for tungsten has resulted in the exploitation of low-grade, disseminated and complex ores, which can solely be processed by the froth flotation method.

Froth flotation is widely used to concentrate metal-bearing minerals: every year, more than 2 billion tons of ores, *i.e.*, most metallic ores except iron ores, are processed by flotation. This method is based on the difference in wettability between minerals surfaces, which induces the attachment of mineral particles to air bubbles evolving in an aqueous phase. The significant difference in electronegativity between mineral cations and anions implies that most minerals exhibit naturally hydrophilic surfaces [33–35]. This is why surfactants, called flotation collectors, are generally used to render the surfaces of the target, *i.e.*, the metal-bearing mineral, hydrophobic and then to recover it in the froth phase. Flotation collectors are traditionally composed of long aliphatic chains along with one or more polar groups that

adsorb on the mineral surface. Fatty acids are generally used for scheelite flotation because of their high affinity for calcium atoms, allowing high recovery, low cost, environmental friendliness, and ease of use [25,36–40]. However, scheelite is associated with other calcium salt-type minerals in most ores, resulting in low adsorption selectivity and, therefore, poor flotation performance [41–44]. In particular, fluorite is the most problematic mineral for the selective scheelite flotation [25], which currently constitutes a technical and scientific challenge. Fortunately, this issue can be overcome by finely tuning the collector and depressants formulations [29,30,45], which should be based on a thorough and accurate description of the adsorption mechanisms at play at the liquid/solid interface [46–51]. Before the addition of the surfactant, minerals are milled and conditioned in the aqueous phase, which means that water molecules are already adsorbed on the surfaces. It is well accepted that surfactants are adsorbed by desorbing a pre-adsorbed water molecules from the mineral surface, according to the Langmuir-type adsorption isotherms [38,52]. Hence, a precise and comprehensive description of the hydration state of minerals whose separation is problematic is required to obtain satisfactory flotation performance. In the presence of liquid water, the affinity of the surface for water depends on the temperature and the adsorbate-adsorbent interaction energy, which is traditionally called indifferently “isosteric heat of adsorption” or “isosteric enthalpy of adsorption” [53]. This quantity can be determined either by experiments or by molecular simulations [54]. Although the heat released during the adsorption process can be measured directly by some calorimetric-volumetric systems [54,55], the most common way to determine this quantity is an indirect method using adsorption isotherms. In such approaches, the isosteric enthalpy of adsorption is assessed from two (or more) adsorption isotherms at close temperatures, which are usually obtained by gas adsorption measurements [53]. To the best of our knowledge, the hydration mechanisms of fluorite ($CaF_2$) have been extensively investigated [56–59] while those of scheelite were poorly studied. Cooper and de

Leeuw (2003) reported average molecular adsorption energies ranging from -22 $kJ \cdot mol^{-1}$ on the less reactive (001) surface to -78 $kJ \cdot mol^{-1}$ on the most reactive (103) surface by means of interatomic potential methods, for a single water molecule [60].

In this study, we investigated the adsorption of water molecules on scheelite using manometric gas sorption experiments combined with *ab initio* molecular dynamics (AIMD) simulations, including a correction for dispersive interactions. AIMD simulations are currently among the most powerful methods used for the description of surface phenomena, in terms of efficiency, accuracy, and computational cost [48,61–65]. The isosteric enthalpy of adsorption has been used as the value to link experimental and theoretical results, since it can be determined by both methods. The global aim of this work was to evaluate the hydration mechanisms on scheelite surfaces and the energies linked to water adsorption, considering surface coverage and temperature, as a basis for further studies on the adsorption of flotation reagents on these surfaces.

## 2. Material and methods

### 2.1 Material

The adsorption experiments were performed on pure scheelite ($CaWO_4$) acquired from China and supplied by the company Minerama. To assess the purity of this mineral, chemical analyses were conducted using inductively coupled plasma-atomic emission spectrometry (ICP-AES) for major elements, inductively coupled plasma-mass spectrometer (ICP-MS) for tungsten, and ion-sensitive electrode (ISE) for fluorine. Scheelite was coarsely crushed by hand in an agate mortar, dry sieved and subsequently ground for 30 min in a planetary mill to maximize the specific surface area and, therefore, the amount of water adsorbed. After milling, the particle size distribution (PSD) of scheelite was measured by laser diffraction

using a Mastersizer Hydro 3000 analyzer (Malvern instruments Ltd.) equipped with a Hydro LV sampler and a measurement cell for liquid phase suspensions.

### 2.2 Adsorption experiments

*Specific surface area*

The textural characteristics of the sample were determined by $N_2$ adsorption at 77 K in a 3-Flex automatic device supplied by Micromeritics. The data treatment of the adsorption isotherms was performed with the Microactive software® also provided by Micromeritics. The BET area, $A_{BET}$ ($m^2 \cdot g^{-1}$), was calculated in the adequate pressure range, taking into account the Rouquerol criterion [66].

*Water adsorption isotherms*

The high-resolution water isotherms were measured at three temperatures (*i.e.*, 275, 283, and 293 K) and up to the saturation pressure in the 3-Flex device. Ultra-pure water (> 18 MΩ.cm) was used as the vapor source. Samples were outgassed overnight at 623 K before being weighed, and an additional outgassing was carried out at the analysis ports at 623 K and under high vacuum for more than eight hours. The measurement of cold and warm volumes was performed after the adsorption-desorption experiments to avoid any unwanted helium entrapment in narrow pores.

### 2.3 Calculation of the isosteric enthalpy of adsorption

The "isosteric heat of adsorption", $Q_{st}$, or the "isosteric enthalpy of adsorption", $\Delta H_{ads}$, used indiscriminately, describes the affinity between the adsorbate and the adsorbent. Since $Q_{st}$ is a heat, it is a positive quantity while, for a spontaneous adsorption process, $\Delta H_{ads}$ is negative, in short $\Delta H_{ads} = -Q_{st}$ [67,68]. The isosteric enthalpy of adsorption is defined as the heat involved, most of the time released, when a molecule adsorbs on a surface, at a given surface occupancy

[69]. Hence, this quantity is negative for most adsorption processes and is equal, for a physisorption process without activation barrier, to the opposite of the isosteric enthalpy of desorption. The isosteric enthalpy of adsorption can be calculated from two (or more) adsorption isotherms acquired in a limited temperature range to avoid artificially introducing errors in the calculation. Once the isotherms are acquired, $\Delta H_{ads}$ can be derived from pressure ($p$)-uptake ($n$) data pairs with the same uptake $n$ at each temperature [53], which is based on the Clausius-Clapeyron equation, as follows:

$$\Delta H_{ads}(n) = -\mathrm{R} \cdot \ln\left(\frac{p_2}{p_1}\right)\frac{T_1 \cdot T_2}{(T_2 - T_1)} \quad (1)$$

where $\Delta H_{ads}(n)$, $T_1$, $T_2$, $p_1$, $p_2$, $n$, and R are the isosteric enthalpy of adsorption ($\mathrm{J \cdot mol^{-1}}$) at a given uptake, the temperatures (K), the equilibrium pressures (bar), the uptake ($\mathrm{mol \cdot kg^{-1}}$), and the ideal gas constant (8.314 $\mathrm{J \cdot mol^{-1} \cdot K^{-1}}$), respectively. Considering the Clausius-Clapeyron equation, the isosteric enthalpy of adsorption is the slope of the curve expressing ln($p$) as a function of (1/$T$) for a given uptake $n$, and can therefore be calculated either on experimental isotherms or on fitted isotherms, although the latter is more recommended [53].

### *2.3.1 From experimental data*

The main problem using experimental data is to determine the accurate experimental pressure at a selected uptake. Indeed, the Clausius-Clapeyron equation allows determining the isosteric enthalpy of adsorption, *i.e.*, the enthalpy of adsorption at a given surface coverage. However, isotherms are experimental quantities measured discretely, *i.e.*, point by point. In order to be able to determine the equilibrium pressure at each given uptake, the three isotherms were interpolated between experimental points using cubic-spline functions. Then, the uptakes range was discretized and, for each point, the isosteric enthalpy of adsorption was calculated using the Clausius-Clapeyron equation, by expressing ln($p$) as a function of (1/$T$) on the

isotherms. Considering the significant error on the adsorbed quantity for the points at low adsorption pressures for the isotherm at 275 K, the latter was not included in the above-mentioned procedure.

### *2.3.2 From fitted adsorption models*

Besides, the experimental data can be fitted with well-known classical adsorption models [53,70], *e.g.*, Langmuir [71], Toth [72], Sips [73] or Freundlich-Langmuir [74], among others, which relate the adsorption quantities to the equilibrium pressures. Considering the shape of the isotherms thus obtained, the Langmuir model [71] was selected as a first approximation to fit the experimental data at low equilibrium pressure. The Langmuir isotherm describes the formation of a single monolayer assuming energy-equivalent adsorption sites and no interaction between adsorbed molecules. It can be expressed as follows [71]:

$$n = \frac{A \cdot B \cdot p}{1 + B \cdot p} \tag{2}$$

where $n$ is the adsorbed quantity (mol·kg$^{-1}$), $A$ (mol·kg$^{-1}$) is the maximum adsorption capacity and $B$ (bar$^{-1}$) is the affinity constant between the adsorbent and the adsorbate and $p$ (bar) is again the equilibrium pressure. However, the Langmuir model exhibits an asymptote that corresponds to an adsorbed monolayer at high equilibrium pressures, which is not displayed in the isotherms obtained for water adsorption on scheelite. Hence, the fitting procedure was improved by choosing a Freundlich-Langmuir model to fit the experimental data over the full range of pressures [53,70,74]. It reads:

$$n = \frac{a \cdot b \cdot p^c}{1 + b \cdot p^c} \tag{3}$$

where $n$ and $p$ have the same meaning as before, $a$ (mol·kg$^{-1}$) is the maximal uptake, $b$ (bar$^{-c}$) is the affinity constant between the adsorbent and the adsorbate, and $c$ (dimensionless) is the

heterogeneity exponent. This model provides the good accuracy of the Langmuir model at low pressures without the limitation of the monolayer at higher equilibrium pressures, whose behavior is well described by the Freundlich model. A common approach applied to improve the fit of the Freundlich-Langmuir model is to assume the existence of two types of sites on the adsorbent surface [53]. As a salt-type mineral, scheelite exhibits $Ca^{2+}$ and $WO_4^{2-}$ on its surfaces, which represent two different adsorption sites with, possibly, two different affinities for water. Therefore, we considered a dual-site Freundlich-Langmuir (DSFL) fit instead of a simple Freundlich-Langmuir (FL) to further improve the fitting procedure and, consequently, the calculation of the isosteric enthalpy of adsorption [53,71,74]. The dual-site Freundlich-Langmuir equation can be expressed as follows [53]:

$$n = \frac{a_1 \cdot b_1 \cdot p^{c1}}{1 + b_1 \cdot p^{c1}} + \frac{a_2 \cdot b_2 \cdot p^{c2}}{1 + b_2 \cdot p^{c2}} \quad (4)$$

where the different terms have the same meaning as in Eq. 3.

For the three models described above, the three experimental isotherms performed at 275, 283, and 293 K were fitted by a least squares fitting procedure using the Levenberg-Marquardt method [75,76] as implemented in SciPy [77]. An analysis of variance (ANOVA) was performed on each fit to assess its validity and its accuracy, through the *p*-value of the model and the root mean square error (RMSE). After the fitting, the equations of the models were rearranged to express the pressure as a function of the uptake and the model parameters. The range of experimental uptakes was discretized to 10 000 points and, for each uptake, the corresponding equilibrium pressure was calculated at each temperature. For Eq. 4, however, the rearrangement was not mathematically straightforward. Therefore, the range of experimental pressures was discretized to 10 000 points and, for each pressure, the corresponding uptake was calculated using the fitted model. Then, the range of experimental uptakes was also discretized to 10 000 points and, for each uptake, the corresponding

equilibrium pressure was calculated using a linear interpolation between the adsorbed quantities determined before. The isosteric enthalpy of adsorption was then calculated using Eq. 1. As was done in the previous sub-section, given the significant error on the adsorbed quantity for the points at low adsorption pressures for the isotherm at 275 K, the latter was not included in the procedure. $\Delta H_{ads}$ was calculated for all the uptake values sampled on the experimental uptakes range, which could be transformed into a surface coverage using the following equation:

$$\theta = \frac{q_{eq} \cdot N_A}{1000 \cdot A_{BET}} \quad (5)$$

where $\theta$ ($nm^{-2}$) is the surface coverage, $q_{eq}$ ($mol \cdot kg^{-1}$) is the adsorbed quantity, $N_A$ ($6.022 \times 10^{23} \cdot mol^{-1}$) is the Avogadro number, and $A_{BET}$ ($nm^2 \cdot g^{-1}$) is the specific area calculated by the BET method. This definition of the surface coverage allows avoiding the influence of the molecular cross-section on the coverage and facilitates the comparison with the atomistic results.

## 2.4 Atomistic simulations

### *2.4.1 Structural models*

For DFT calculations, a primitive tetragonal cell of $CaWO_4$ was generated from experimental lattice parameters $a_{Sch} = b_{Sch} = 5.24$ Å and $c_{Sch} = 11.37$ Å [78]. After being relaxed in terms of ion positions, cell shape, and cell size by DFT calculations, the lattice parameters of the primitive scheelite cell were $a_{Sch} = b_{Sch} = 5.21$ Å and $c_{Sch} = 11.34$ Å (with all angles at 90°), which are very close the aforementioned experimental parameters. This fully-relaxed primitive cell was subsequently used to create the (001) and the (112) surfaces, which represent the most exposed for $CaWO_4$, as reported by experimental and theoretical studies [34,60,79,80]. Then, a supercell containing 192 atoms (32 Ca, 32 W, and 128 O) was

generated for each surface, comprising four layers of calcium/tungsten atoms, each of them separated by two or four successive layers of oxygen atoms for (001) and (112) surfaces, respectively (Figure 1). For each of the (001) and (112) surfaces, when the slab was created, due to the periodic boundary conditions, two reciprocal surfaces were generated. Considering the bond breakage procedure, the two surfaces were equivalent in terms of density of broken bonds and were exactly similar, which avoided the existence of any dipole moment in the slab and in the cell. The (001) surface consists of a plane of four six-coordinated calcium atoms and four tungstate anions ($WO_4^{2-}$) that, considering the high energy of the W-O bond compared to the Ca-O bond [81], remain unbroken during the cleavage process (Figure 1). Besides, the (112) surface consists of a plane of eight six-coordinated calcium atoms along with eight tungstate ions, which also remain unbroken during the cleavage process (Figure 1). On the (001) surface, the calcium atoms are separated by 5.21 Å in all directions while they are separated by 3.86 Å in one direction on the (112) surface. On both (001) and (112) scheelite surfaces, the calcium atoms are six-coordinated while they are eight-coordinated in the scheelite lattice, entailing two dangling bonds per calcium atom. To avoid any unwanted interaction due to the periodicity of the cells, the latter were constructed so that a vacuum zone of 15 Å was systematically kept between the surface and the upper limit of the cell along the z-axis. One layer of atoms at the bottom of the cell were frozen at their bulk positions. As *ab initio* molecular dynamics simulations are numerically costly, in this case the slabs were reduced to a thickness of two calcium layers, *i.e.*, 96 atoms. The cell parameters and number of atoms for each surface and simulation type, static DFT or AIMD, are summarized in Table 1.

Table 1. Cell parameters (including vacuum) and number of atoms for each simulation type and for each surface.

| Surface | Simulation type | Atoms | Cell parameters |
|---|---|---|---|
| (001) | Static DFT | 192 | a = b = 10.42 Å; c = 5.67 Å + 15 Å vacuum<br>α = β = γ = 90° |
| | AIMD | 96 | a = b = 10.42 Å; c = 2.84 Å + 15 Å vacuum<br>α = β = γ = 90° |
| (112) | Static DFT | 192 | a = 7.37 Å, b = 15.41 Å, c = 12.31 Å + 15 Å vacuum<br>α = β = 90°; γ = 118.57° |
| | AIMD | 96 | a = 7.37 Å, b = 15.41 Å, c = 6.87 Å + 15 Å vacuum<br>α = β = 90°; γ = 118.57° |

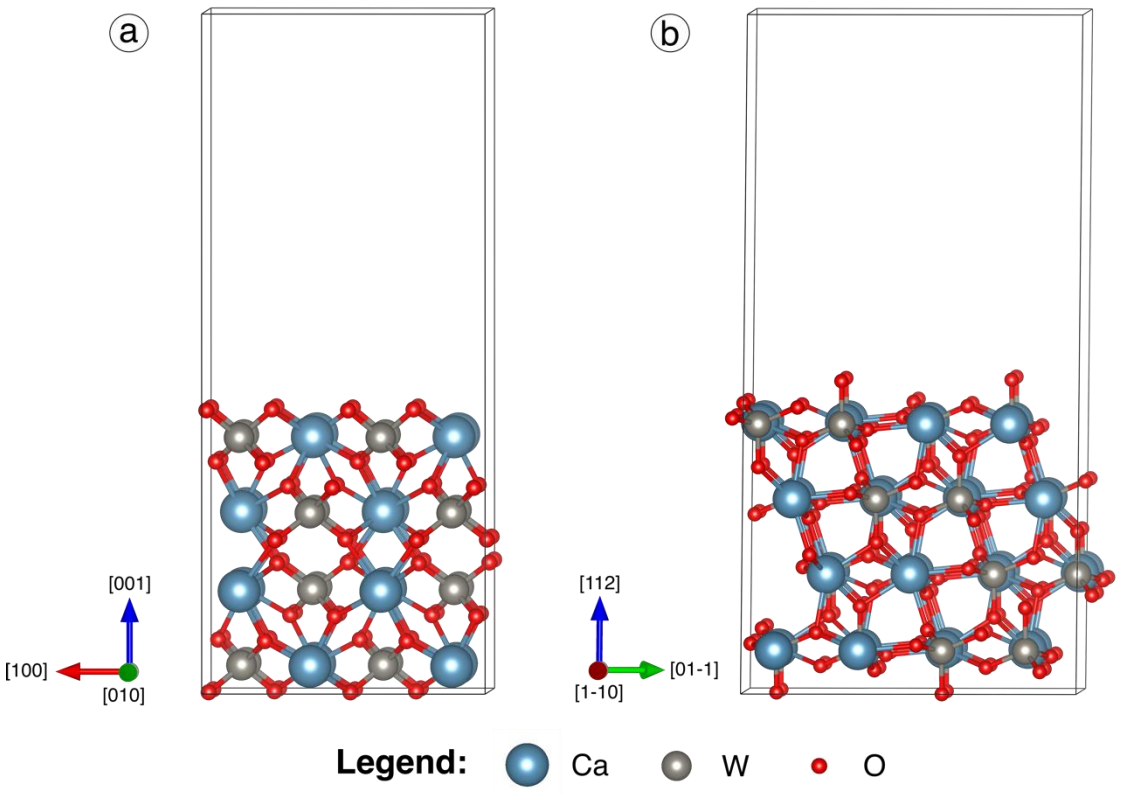



Figure 1. Side views of cells containing scheelite surfaces (001) (a) and (112) (b), used for the static DFT calculations. For AIMD simulations, the slabs were reduced to two layers of calcium atoms instead of the four layers represented here.

### *2.4.2 Computational details*

All the DFT calculations were carried out using the VASP package [82]. We employed the PBE exchange-correlation functional of Perdew and co-workers [83] in the generalized gradient approximation. Also, the electron-ion interactions were described using the PAW method [84,85] with a plane wave kinetic energy cut-off of 500 eV and an electron density cut-off of 600 eV. However, the first relaxation of the primitive scheelite cell, before generating the two surfaces, was performed with a planewave kinetic energy cut-off of 1 000 eV. The following valence electrons were considered: $1s^1$ for hydrogen, $3s^2$ $3p^6$ $4s^2$ for

calcium, $2s^2\ 2p^4$ for oxygen, and $5s^2\ 5p^6\ 6s^2\ 5d^4$ for tungsten. The Kohn-Sham equations [86] were solved self-consistently [87] until the energy difference between the cycles became lower than $10^{-8}$ eV. All the calculations were realized by sampling the Brillouin zone at the Gamma point, considering the large size of the cells and according to preliminary calculations. The structural relaxations were carried out until all forces were smaller than 0.01 eV·Å$^{-1}$. Moreover, the D2 correction of Grimme was systematically included to take dispersion forces into account [88]. Besides, for *ab initio* molecular dynamics (AIMD) simulations, considering their computational cost, the convergence parameter for the self-consistently-solved Kohn-Sham equations and the planewave kinetic energy cut-off were reduced to $10^{-5}$ eV and 400 eV, respectively. The AIMD simulations were conducted using a Nosé-Hoover thermostat [89,90] with a temperature of 300 K and a timestep of 1 fs.

### 2.4.3 Calculation of the adsorption energies

The adsorption energies were calculated by subtracting the energies of the bare surface and of the isolated water molecule(s) from the energy of the system with the molecule(s) adsorbed, as follows:

$$\Delta E_{ads} = E_{Scheelite-W} - E_{Scheelite} - n\ x\ E_W \quad (6)$$

where $E_{Scheelite\text{-}W}$, $E_{Scheelite}$, $E_W$, and $n$ are the energy of the scheelite slab with the water molecule(s) adsorbed, the energy of the bare scheelite slab, the energy of the single water molecule in gas phase, and the number of water molecules, respectively. The contribution of dispersion energy to the adsorption energy was determined using Eq. 6, in which the energy was only the contribution of the dispersion energy to the total energy instead of the total energy itself. For the substitution of $WO_4^{2-}$ by 2 $HO^-$ at the scheelite surface, the following reaction was considered for only one spatial configuration:

$$CaWO_4\ (surface) + 2\ H_2O \rightarrow Ca(OH)_2\ (surface) + WO_3{,}H_2O \quad (7)$$

The reaction energy for this reaction was calculated by subtracting the sum of the energies of the reagents from the sum of the energies of the products, calculated in vacuum conditions. The system *Ca(OH)$_2$ (surface)* corresponds to the scheelite slab where a $WO_4^{2-}$ anion has been substituted by two $OH^-$ ions.

The adsorption enthalpies of water at 300 K were computed using the aforementioned method, by averaging the energy of each system over the 100 picoseconds of the AIMD simulation, excluding a thermalization period of 10 ps. This can be done since the volume and pressure variations are negligible during the adsorption process, which implies that the variation of enthalpies are equivalent to the variation of internal energies extracted from AIMD simulations. Besides, our objective was to determine an isosteric enthalpy of adsorption by AIMD simulations to compare it to the experimental data, which requires a successive addition of water molecules. The coverage was therefore gradually increased, and an AIMD simulation was performed for each considered coverage. In AIMD simulations, the isosteric enthalpy of adsorption, $\Delta H_{ads}$, corresponds of the molecular adsorption energy when a given number of molecules is added to the surface, without considering the adsorption energies of the previously adsorbed molecules. Hence, for a coverage of $x$ water molecules, $\Delta H_{ads}$ was calculated as follows:

$$\Delta H_{ads} = \frac{\Delta E_{ads-(x+y)W} - \Delta E_{ads-(x)W}}{y} \quad (8)$$

where $\Delta E_{ads\text{-}xW}$ is the adsorption energy of $x$ water molecules and $\Delta E_{ads\text{-}(x+y)W}$ is the adsorption energy of $x+y$ water molecules, as determined using Eq. 6. $y$ corresponds to the number of added molecules between the two AIMD simulations with two different coverages. For coverages below the monolayer, $y$ was equal to 1, 2, or 4 since coverages of 1, 2, 4, and 8 $H_2O$ were considered, while for coverages above the monolayer, $y$ was equal to 8 since we incremented layer by layer and each layer comprised 8 water molecules.

## 3. Results

### 3.1 Experimental results

Scheelite was pure at 97.65% with a slight contamination by quartz and apatite (Table 2).

Table 2. Chemical composition of scheelite analyzed by ICP-AES, ICP-MS, and ion-sensitive electrode. <D.L. = Lower than detection limit.

| CaO (wt.%) | $P_2O_5$ (wt.%) | $SiO_2$ (wt.%) | MgO (wt.%) | $Al_2O_3$ (wt.%) | $Fe_2O_3$ (wt.%) | $Na_2O$ (wt.%) | $K_2O$ (wt.%) | $TiO_2$ (wt.%) | MnO (wt.%) | W (wt.%) | F (wt.%) |
|---|---|---|---|---|---|---|---|---|---|---|---|
| 19.82 | 1.63 | 0.72 | <D.L. | <D.L. | <D.L. | <D.L. | <D.L. | <D.L. | <D.L. | 63.71 | <D.L. |

The obtained PSD, which was the average of 4 successive measurements, is presented in Figure 2. The characteristic sizes $d_{90}$, $d_{50}$, and $d_{10}$, which correspond to the diameters below which 90, 50 and 10% of the particles can be found, respectively, were calculated as averages of the different measurements. Their values were 24.3 ± 0.29 µm, 10.9 ± 0.18 µm, and 2.9 ± 0.08 µm, respectively.

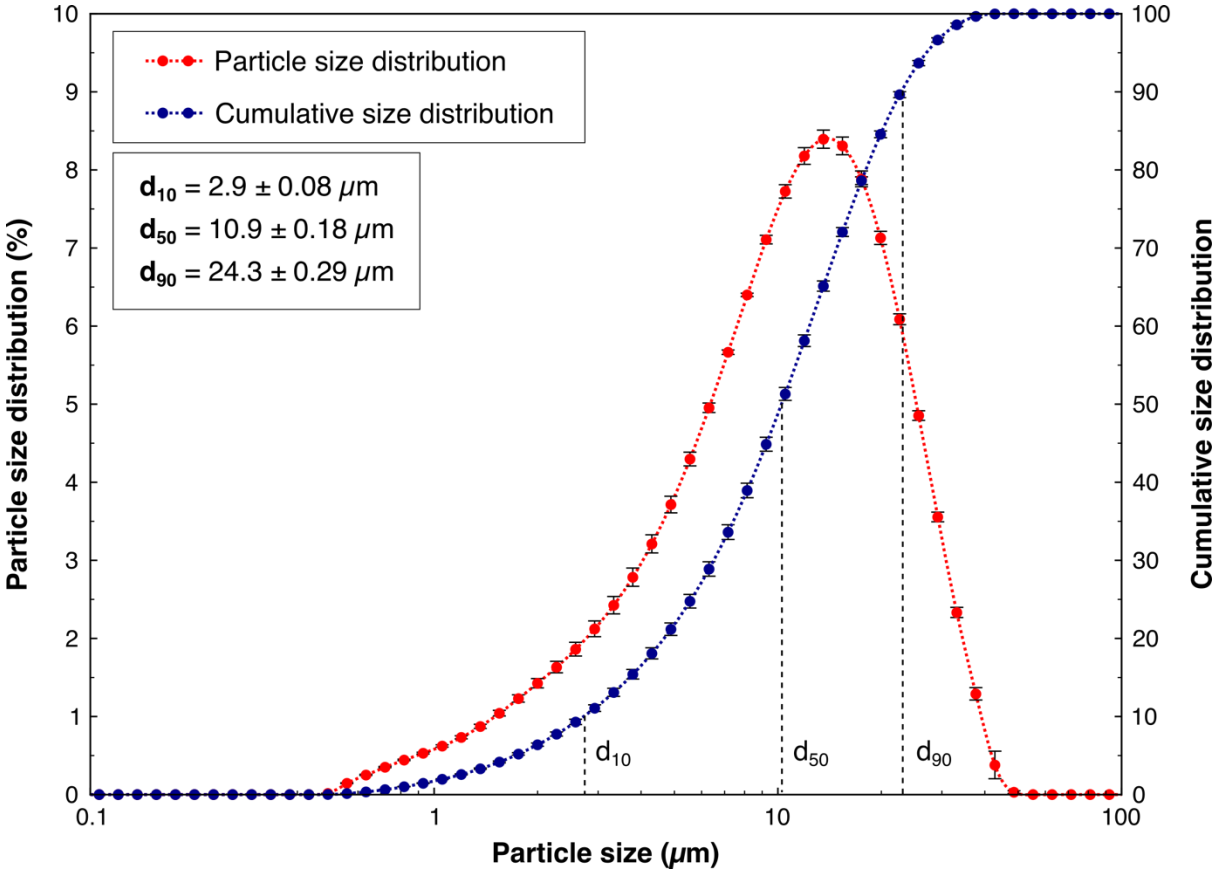



Figure 2. Particle size distribution and cumulative size distribution of scheelite used for adsorption experiments. $d_{90}$, $d_{50}$, and $d_{10}$ correspond to the diameters below which 90, 50 and 10% of the particles can be found, respectively.

### 3.1.1 Adsorption isotherms

Nitrogen adsorption at 77K on scheelite allowed to determine an $A_{BET}$ of 0.85 $m^2 \cdot g^{-1}$. Although this surface area is rather small, the accuracy of this determination was validated by carrying out the adsorption experiment 3 times, the reported value being the average of the three surface area determinations with a variance smaller than 5%. We also carried out Kr isotherms at 77 K on the same sample, leading to similar results, which confirmed the accuracy of the former measurements.

The water adsorption isotherms at the three temperatures considered, *i.e.*, 275, 283, and 293 K, are shown in Figure 3. At low equilibrium pressure ($p$ < 1 mbar), the amount adsorbed

increases significantly with pressure before reaching a knee, after which the amount adsorbed rises slowly with pressure. At high pressure, water condensation occurs, both on the tube of the sample holder and on the sample. According to the literature, this is a typical type II isotherm, which corresponds to a significantly high adsorption energy of molecules on a non-porous material [91]. The uptake values at low pressure correspond to the adsorption of the first water monolayer on the scheelite surface, with a high adsorption enthalpy, while the rest of the isotherm represents the progressive formation of multilayers, with a lower adsorption enthalpy tending towards the enthalpy of water condensation. Obtaining a type II isotherm is consistent with the crystallographic structure of scheelite, which does not exhibit nano-sized pores, and the good crystallinity of the sample, which does not exhibit micrometer-sized pores. Besides, the significant affinity of the scheelite surfaces for water at low pressure is consistent with the considerable polar nature of scheelite, which consists of an assembly of $WO_4^{2-}$ anions and $Ca^{2+}$ cations (Figure 1).

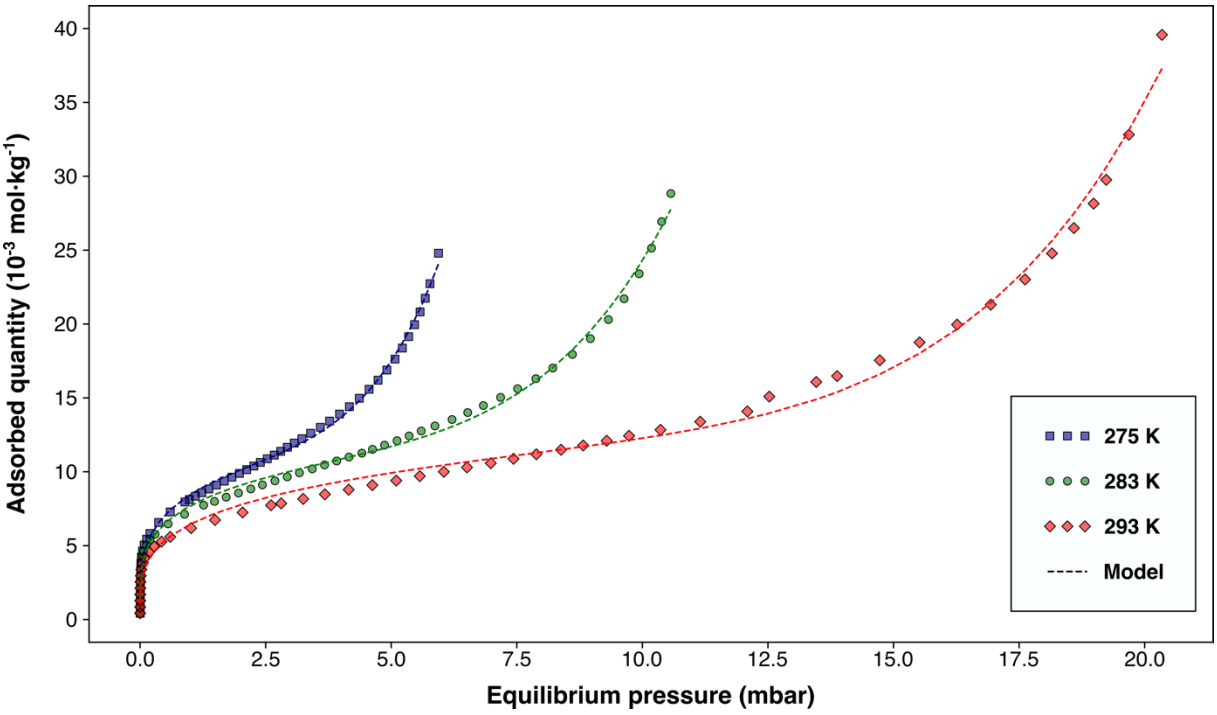



Figure 3. Adsorption isotherms of gas water on scheelite at 275, 283, and 293 K (dots) and their fits with the Dual-Site Freundlich-Langmuir model (Eq. 4, dashed lines).

### 3.1.2 Isosteric enthalpy of adsorption from experimental data

For each isotherm, the curve was interpolated between experimental points using cubic-spline functions. Only points with an adsorbed quantity higher than $5 \cdot 10^{-3}$ mol·kg$^{-1}$ were included in the fitting procedure due to the low accuracy of the experimental values measured at very low equilibrium pressures. The isosteric enthalpy of adsorption, calculated by the Clausius-Clapeyron method and expressed as a function of the adsorbed quantity, is presented in Figure 4. For the points corresponding to the lowest adsorbed amounts, the calculated isosteric enthalpy of adsorption is around -65 kJ·mol$^{-1}$. However, considering Eq. 5, an adsorbed quantity of $5 \cdot 10^{-3}$ mol·kg$^{-1}$ represents a surface coverage of around 3.5 molecules·nm$^{-2}$. For the (001) and (112) surfaces, the surface densities of calcium sites, calculated from our atomistic structural models, are 3.7 and 4.1 calcium atoms·nm$^{-2}$, respectively. This implies that, at an adsorbed quantity of $5.10^{-3}$ mol·kg$^{-1}$, all the calcium atoms of both surfaces are saturated, *i.e.*, a monolayer is already formed. Hence, the direct use of experimental data does not describe accurately the adsorption of the first molecules on the scheelite surface. Therefore, to have access to very low coverages, the fitting procedure was performed using models.

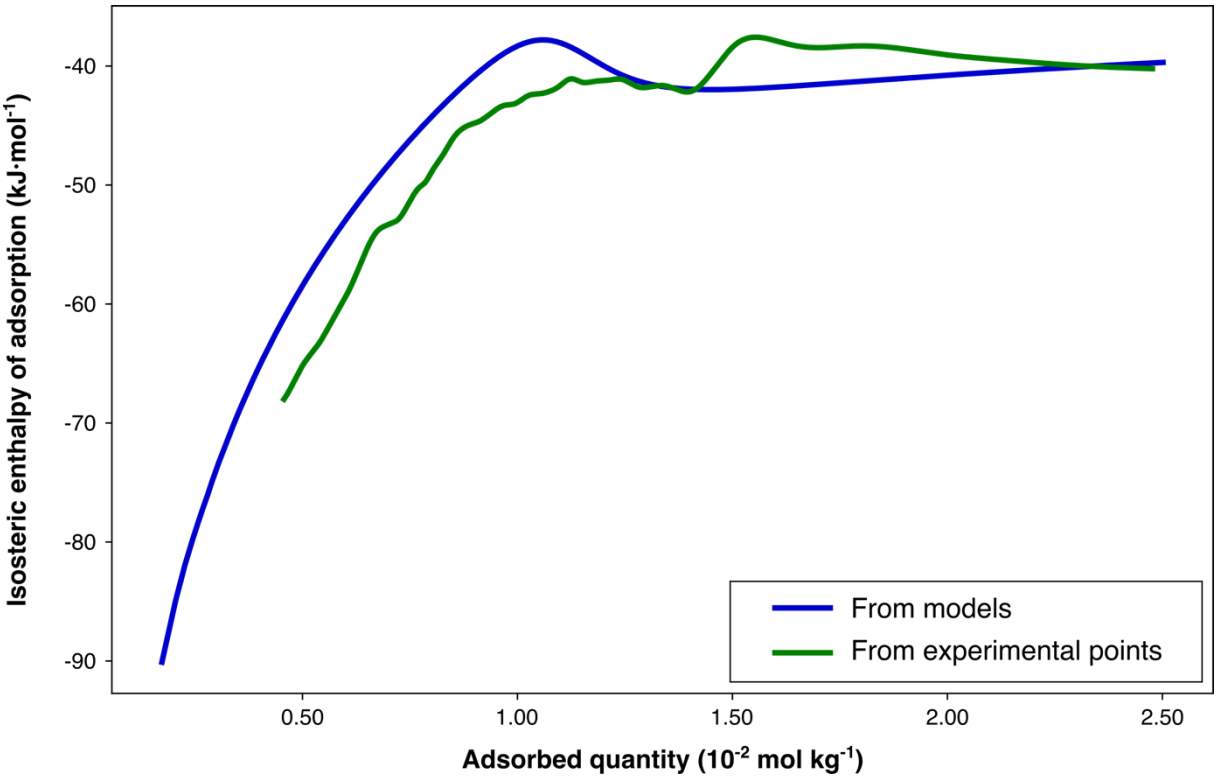



Figure 4. Isosteric enthalpy of water vapour adsorption on scheelite as a function of the adsorbed quantity, determined directly from experimental points (green curve) and from the model (eq. 4) fitted to the experimental points (blue curve).

### *3.1.3* Isosteric enthalpy of adsorption from models

The most reliable option to calculate the isosteric enthalpy of adsorption is to use a model that fits the experimental data to determine the pairs of values (pressure, uptake) required for the Clausius-Clapeyron method. First of all, at low to medium equilibrium pressures, the isotherms exhibit a behavior similar to a Langmuir isotherm, *i.e.*, a significant increase of the adsorbed amounts followed by a plateau. Since only the first part of the isotherms is of interest to describe the water/scheelite interactions, the isotherms can be fitted in first approximation by a Langmuir model, considering only the uptakes lower than 0.01 mol·kg$^{-1}$. Although the uptakes at very low pressure are accurately described, the points that correspond to the plateau are poorly described since the isotherms do not exhibit a strict asymptote as the

Langmuir model does. Therefore, the fitting was improved by using a Freundlich-Langmuir isotherm, which better describes the absence of asymptote once the plateau is reached, due to the multilayer formation. Finally, the fitting was further improved by using a dual-site Freundlich-Langmuir (DSFL) isotherm for the whole range of experimental pressures. Table 3 summarizes the results of the fits, including the determination coefficient $R^2$, the root mean square error (RMSE), and the *p*-value of the model, for each isotherm.

Table 3. Results of the fits for each model (Langmuir, Freundlich-Langmuir, and Dual-Site Freundlich-Langmuir) and for each isotherm (at 275, 283, and 293 K).

| | Range of uptakes | *T* (K) | $R^2$ | RMSE ($\times 10^{-3}$) | *p*-value |
|---|---|---|---|---|---|
| Langmuir | 0-0.01 mol·kg$^{-1}$ | 275 | 0.97 | 1.03 | < 0.001 |
| | 0-0.01 mol·kg$^{-1}$ | 283 | 0.96 | 1.30 | < 0.001 |
| | 0-0.01 mol·kg$^{-1}$ | 293 | 0.95 | 1.37 | < 0.001 |
| Freundlich-Langmuir | 0-0.01 mol·kg$^{-1}$ | 275 | 0.99 | 0.61 | < 0.001 |
| | 0-0.01 mol·kg$^{-1}$ | 283 | 0.99 | 0.56 | < 0.001 |
| | 0-0.01 mol·kg$^{-1}$ | 293 | 0.99 | 0.51 | < 0.001 |
| Dual-Site Freundlich-Langmuir | Whole | 275 | 1.00 | 0.44 | < 0.001 |
| | Whole | 283 | 1.00 | 0.47 | < 0.001 |
| | Whole | 293 | 1.00 | 0.69 | < 0.001 |

The DSFL isotherm satisfactorily fitted the experimental data (Figure 3) and, was therefore selected for the calculation of the isosteric enthalpy of adsorption (Figure 4). The fitting procedure was performed over the whole experimental range, without extrapolating to lower uptakes than those measured. The point of lowest uptake represents $2 \cdot 10^{-3}$ mol·kg$^{-1}$ of water adsorbed on scheelite, which corresponds to a coverage of 1.4 molecules·nm$^{-2}$. On average, the water molecules are therefore roughly separated by 1 nm from each other on the surface, which means that they do not interact. Hence, we can consider that the points with the lowest

adsorbed quantity describe the adsorption of isolated water molecules onto the scheelite surface. For these points, the calculated adsorption enthalpy is around -90 $kJ \cdot mol^{-1}$. This value is consistent with the typical absolute values for the adsorption/desorption of the first water molecules from metals/minerals surfaces [92], *e.g.* -89 $kJ \cdot mol^{-1}$ for calcite [93] or -55 $kJ \cdot mol^{-1}$ for fluorite [56]. Then, the isosteric enthalpy of adsorption decreases steadily in absolute value with the adsorbed quantity, until reaching the enthalpy of condensation of water, around -42 $kJ \cdot mol^{-1}$. The decrease of the isosteric enthalpy of adsorption corresponds to the formation of multilayers of water molecules on the scheelite surface, which adsorb with lower enthalpies compared to the first monolayer. This can be attributed to the decrease of the influence of the surface on the molecules due to the screening effect of the previous adsorbed layers.

## 3.2 Theoretical results

The adsorption mechanisms of water on scheelite were modelled by increasing gradually the number of water molecules on the surface, from an isolated molecule to a cell full of water molecules representing water condensation.

### 3.2.1 Isolated water molecule on scheelite surfaces

A water molecule can adsorb under dissociated form, under molecular form, or by substituting surface ions. Therefore, as a starting point, the three abovementioned cases were tested at 0 K.

*Under dissociated form*

Several configurations were explored: a hydroxyl group was placed above a calcium ion on the surface, with the O close to the calcium and the H pointing upwards, away from the surface. The lone $H^+$ ion was placed at the vicinity of an oxygen atom forming part of a tungstate ion, with two distances between the OH and H groups tested.

When the $H^+$ and the $HO^-$ were set on an oxygen atom of a tungstate ion and a neighboring calcium atom, respectively, for both (112) and (001) surfaces, the $H^+$ ion was captured by the $HO^-$ group and the water molecule was reformed (Figure 5). This indicates that the adsorption of water under molecular form is favored compared to the adsorption of water under dissociated form. However, significant differences can be observed between the two surfaces: on the (001) surface, the reformed water molecule adsorbed onto a single calcium atom with $d_{Ca\text{-}O}$ = 2.29 Å and established a hydrogen bond with an oxygen atom of the closest tungstate ion with $d_{H\text{-}O}$ = 1.58 Å (Figure 5a). For this configuration, the calculated adsorption energy was $\Delta E_{ads}$ = -87.6 kJ·mol$^{-1}$ including $\Delta E_{disp}$ = -15.2 kJ·mol$^{-1}$, indicating a significantly strong adsorption. On the other hand, on the (112) surface, the reformed water molecule adsorbed between two calcium atoms with Ca-O bond lengths of 2.60 Å and 2.66 Å (Figure 5b). One hydrogen atom of the water molecule was oriented towards the closest oxygen atom with $d_{H\text{-}O}$ = 1.88 Å. This adsorption occurred with $\Delta E_{ads}$ = -127.3 kJ·mol$^{-1}$ including $\Delta E_{disp}$ = -25.2 kJ·mol$^{-1}$, which represents a higher value than for the (001) surface. The difference in terms of adsorption energies between the two surfaces can be attributed to the difference in Ca-Ca distance: on the (112) surface, the calcium atoms are close enough to allow the adsorption of the water molecule between the two, which is impossible on the (001) surface considering the higher Ca-Ca distance. Overall, the high adsorption energies found for both surfaces for the adsorption of a single water molecule are probably induced by the significant reactivity of surface calcium atoms, resulting from the two dangling bonds per calcium atom mentioned above.

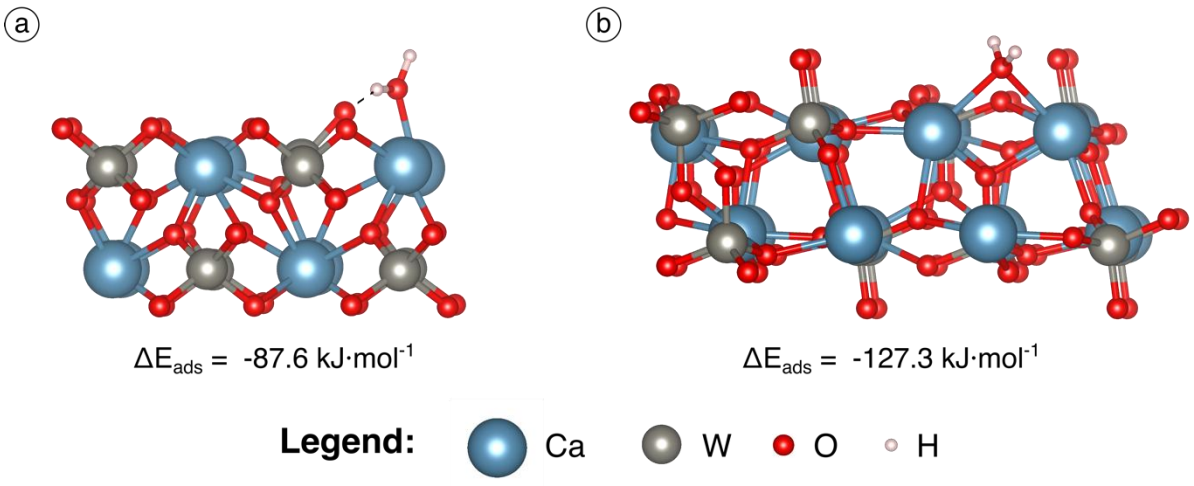



Figure 5. Adsorption of dissociated water molecule with short OH-H distance onto (001) (a) and (112) (b) scheelite surfaces. Only the upper part of the surfaces is displayed here. The dashed lines represent hydrogen bonds.

For both (001) and (112) surfaces, when the proton was placed far from the hydroxyl group (> 6 Å), *i.e.*, without interaction between them, the hydrogen ion formed a H-O bond with an oxygen atom part of a tungstate anion, whose length was 1.01 Å. The H atom established a hydrogen bond with the closest oxygen atom, part of another tungstate ion, with $d_{H\text{-}O}$ ~ 1.70 Å (Figure 6). For the (001) surface, the $HO^-$ ion adsorbed between a calcium atom and a tungsten atom, establishing a Ca-O bond and a W-O bond with $d_{Ca\text{-}O}$ = 2.27 Å and $d_{W\text{-}O}$ = 2.08 Å (Figure 6a). The tungsten was then five-coordinated since it displayed five W-O bonds in this configuration, which is rather unfavorable since the calculated adsorption energy was $\Delta E_{ads}$ = +11.4 kJ·mol$^{-1}$. However, this means that, for a moderate $HO^-$ activity, *i.e.*, a slightly alkaline pH, the water molecule can adsorb under dissociated form onto the (001) scheelite surface. Besides, for the (112) surface, the $HO^-$ ion adsorbed between two calcium atoms (Figure 6b), which is allowed by the fact that, on this surface, they are separated by only 3.86 Å. The lengths of the two created Ca-O bonds were 2.23 Å and 2.26 Å. The calculated adsorption energy for this configuration was $\Delta E_{ads}$ = -47.3 kJ·mol$^{-1}$ including

$\Delta E_{disp}$ = -19.9 kJ·mol$^{-1}$, which indicates that the adsorption of water molecules under their dissociated form is possible spontaneously, albeit much less favored than the adsorption under their molecular form (occurring with $\Delta E_{ads}$ = -127.3 kJ·mol$^{-1}$).

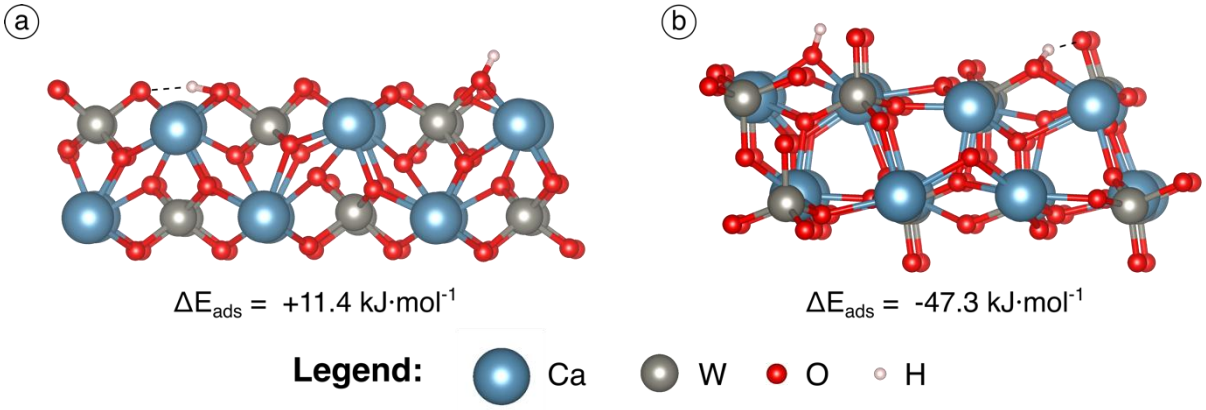



Figure 6. Adsorption of dissociated water molecule with high HO-H distance onto (001) (a) and (112) (b) scheelite surfaces. The (001) surface has been extended to have a large enough distance between the OH group and the H atom. Only the upper part of the surfaces is displayed here. The dashed lines represent hydrogen bonds.

*Under molecular form*

Since molecular adsorption of water appeared to be more stable than dissociative adsorption, a water molecule was set directly above a surface calcium ion. Several configurations were tested, with different orientations of the hydrogen atoms of the water molecule. All input configurations led to the same final geometries. For the (001) surface, the water molecule adsorbed onto a calcium atom with $d_{Ca\text{-}O}$ = 2.29 Å and established a hydrogen bond with an oxygen atom of the closest tungstate ion with $d_{H\text{-}O}$ = 1.58 Å, as described previously when the water molecule was reformed (Figure 5a). The adsorption energies were roughly the same as those given previously, namely $\Delta E_{ads}$ ~ -87 kJ·mol$^{-1}$ including $\Delta E_{disp}$ ~ -15 kJ·mol$^{-1}$. For the (112) surface, the water molecule adsorbed onto a calcium atom with $d_{Ca\text{-}O}$ = 2.45 Å while the two hydrogen atoms established hydrogen bonds with two oxygen atoms from two different

tungstate anions. This configuration resulted in a calculated adsorption energy of $\Delta E_{ads}$ = -102.3 kJ·mol$^{-1}$ including $\Delta E_{disp}$ = -23.1 kJ·mol$^{-1}$, which is significantly lower than when the molecular water is reformed from a dissociated molecule. This can be attributed to a local energy minimum at a higher energy compared to the system where the water molecule is reformed.

*Substitution of $WO_4^{2-}$ by 2 $HO^-$*

Finally, the substitution of $WO_4^{2-}$ by 2 $HO^-$ on the (001) and (112) scheelite surfaces was investigated. Two hydroxyl ions were set at the place of a surface tungstate anion to maintain the electrical neutrality. In the scheelite lattice, tungstate anions are eight-coordinated, *i.e.*, each oxygen atom of the tungstate anion is bonded to two calcium atoms, and the global tungstate anion is bonded to eight different calcium atoms. On both (001) and (112) surfaces, tungstate anions are only six-coordinated, *i.e.*, they are bonded to six different calcium atoms. However, when a tungstate anion is substituted by two $HO^-$ ions, the latter cannot establish six Ca-O bonds due to their small size compared to a $WO_4^{2-}$ anion. Hence, the substitution reaction was highly endothermic, with $\Delta E_r$ = +424.5 kJ·mol$^{-1}$ for the (112) surface and $\Delta E_r$ = +321.2 kJ·mol$^{-1}$ for the (001) surface. This mechanism seems therefore very unlikely to occur on scheelite surface, which is consistent with the fact that scheelite dissolution is favored at acidic pH rather than at alkaline pH.

### 3.2.2 Towards the full hydration of the scheelite surfaces at 300 K

Once the most favorable configuration for a single molecule of water was determined, the progressive hydration of the surfaces was investigated using AIMD simulations, at 300 K. One, two, four, or eight $H_2O$ molecules were placed on the surfaces composed of four calcium atoms and four tungstate anions. For that study, the (112) surface was reduced to be comparable to the (001) surface that originally consisted of a plane of four calcium atoms.

Both surfaces displayed an area of around 1 $nm^2$, used to calculate the corresponding surface coverage. For the (001) surface, the first four water molecules were placed sequentially on the four surface calcium atoms while the last four molecules were set on tungstate anions, their hydrogen atoms pointing towards the surface. For the (112) surface, the first two water molecules were placed in the most favorable configuration, *i.e.*, each water molecule between two calcium atoms. Each of four other water molecules was set on a calcium atom while the last four molecules were set on tungstate anions, in a similar way to the (001) surface. The evolution of the isosteric enthalpies of adsorption is presented in Figure 7, while the water structures at monolayer and full coverage for the two surfaces are presented in Figure 9 and 9, respectively.

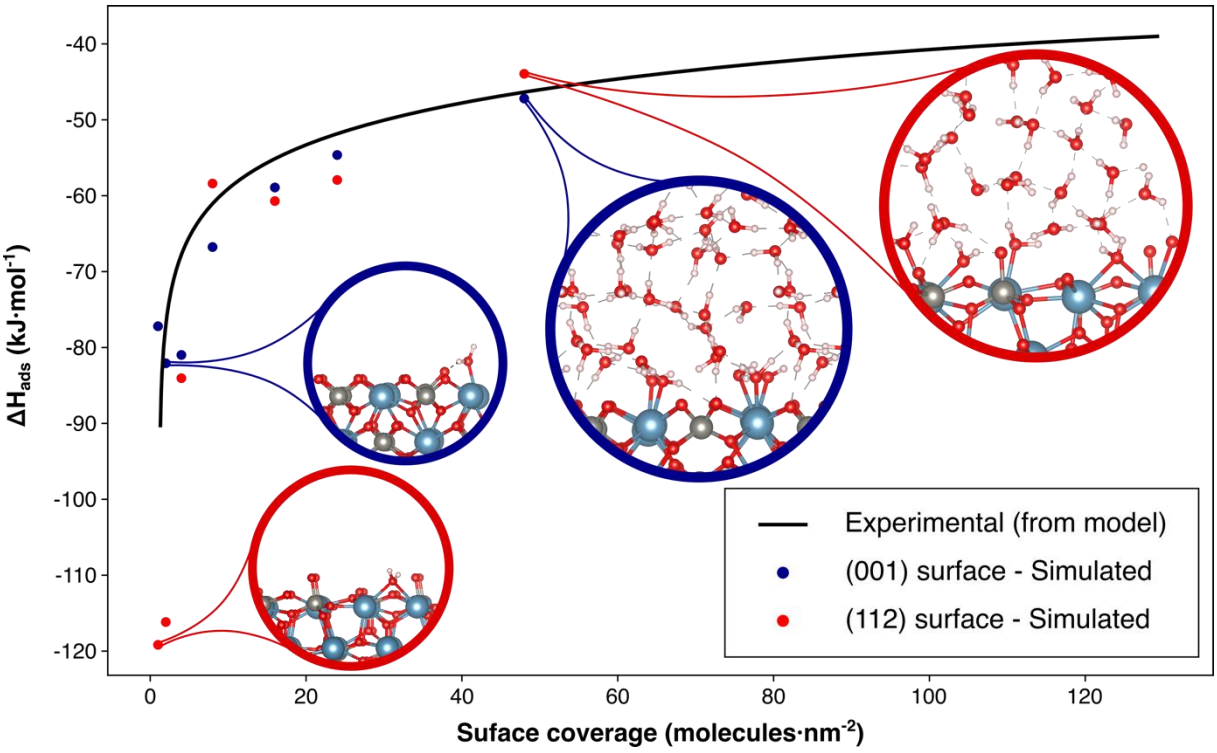



Figure 7. Adsorption energies per water molecule for the (001) and (112) scheelite surfaces when the water coverage is increased from 1 to 48 water molecules (for surfaces of around 1 $nm^2$, which therefore represents a coverage of 1 to 48 $nm^{-2}$).

On the (001) surface, the calculated isosteric enthalpy of adsorption remains constant at around -80 kJ·mol$^{-1}$ for the first four added water molecules (Figure 7). This indicates that the water molecules are far enough apart not to interact and that they adsorb on the same adsorption sites, *i.e.*, on the surface calcium atoms. With the next four water molecules added, thus increasing the total from four to eight molecules, the absolute value of the isosteric enthalpy of adsorption decreases to -67 kJ·mol$^{-1}$ (Figure 7) despite the fact that, at this coverage, the water molecules obviously interact with each other (Figure 8a), which probably significantly increases the adsorption energies.

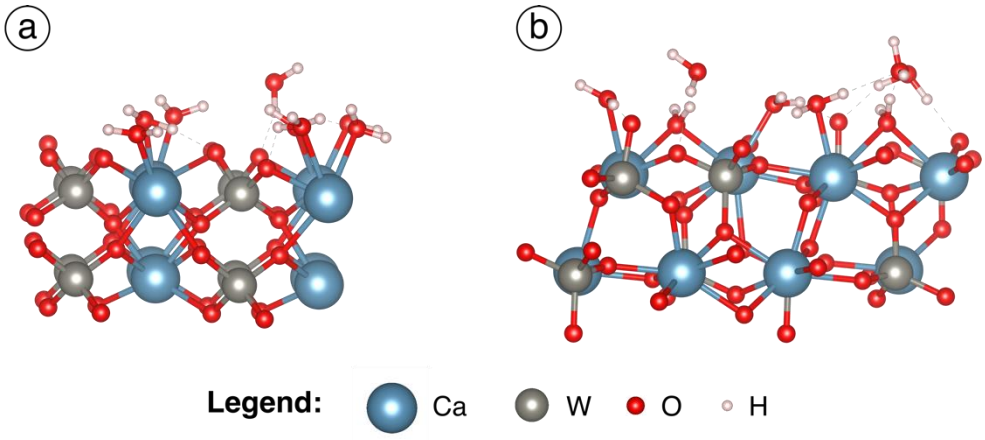



Figure 8. Adsorption of eight water molecules, which corresponded to a monolayer, onto (001) (a) and (112) (b) scheelite surfaces. The dashed lines represent hydrogen bonds.

It is interesting to note that, at this coverage, two water molecules adsorb on the same calcium atom, but with different Ca-O distances, 2.45 Å and 2.84 Å (Figure 8a). Hence, for the complete formation of the first monolayer, each calcium atom is occupied by two adsorbed water molecules (Figure 8a), which is in accordance with the two dangling bonds of the calcium atoms on the surface. The adsorption of two water molecules per calcium atom could explain the decrease in adsorption enthalpies when the coverage is increased. This phenomenon was observed by Cooper and de Leeuw [60], who reported the adsorption of two water molecules on each surface calcium atom of the (001) scheelite surface [60] and average

molecular adsorption energies for a full surface coverage of -22.1 $kJ \cdot mol^{-1}$. The latter value is significantly lower than the values calculated here and is probably due to the use of different methods, since these authors employed interatomic potentials derived from DFT but, strictly speaking, not DFT. Then, by increasing the coverage to two, three, and multiple adsorption layers, the isosteric enthalpies of adsorption decrease and tend towards the enthalpy of water condensation, around -40 $kJ \cdot mol^{-1}$. On the (112) surface, the absolute value of the adsorption energy per water molecule decreases from -116 $kJ \cdot mol^{-1}$ for two molecules to -84 $kJ \cdot mol^{-1}$ for four molecules and to -58 $kJ \cdot mol^{-1}$ for eight molecules (Figure 7). This is probably the result of the change in the adsorption mode. On the one hand, for one or two adsorbed molecules, each molecule is adsorbed between two calcium atoms. On the other hand, when four or eight molecules are present, two molecules are adsorbed between two calcium atoms and one additional molecule is adsorbed on each calcium atom (Figure 8b). Furthermore, among the eight molecules, some adsorb by establishing hydrogen bonds with surface tungstate anions (Figure 8b), which contributes to decrease the absolute value of the adsorption energy per water molecule. Besides, from four water molecules, the average adsorption energy per molecule is the same for the (001) and the (112) surfaces, due to the two above-mentioned phenomena. At this coverage, which is lower than the monolayer, the reactivity differences between the two surfaces are already negligible.

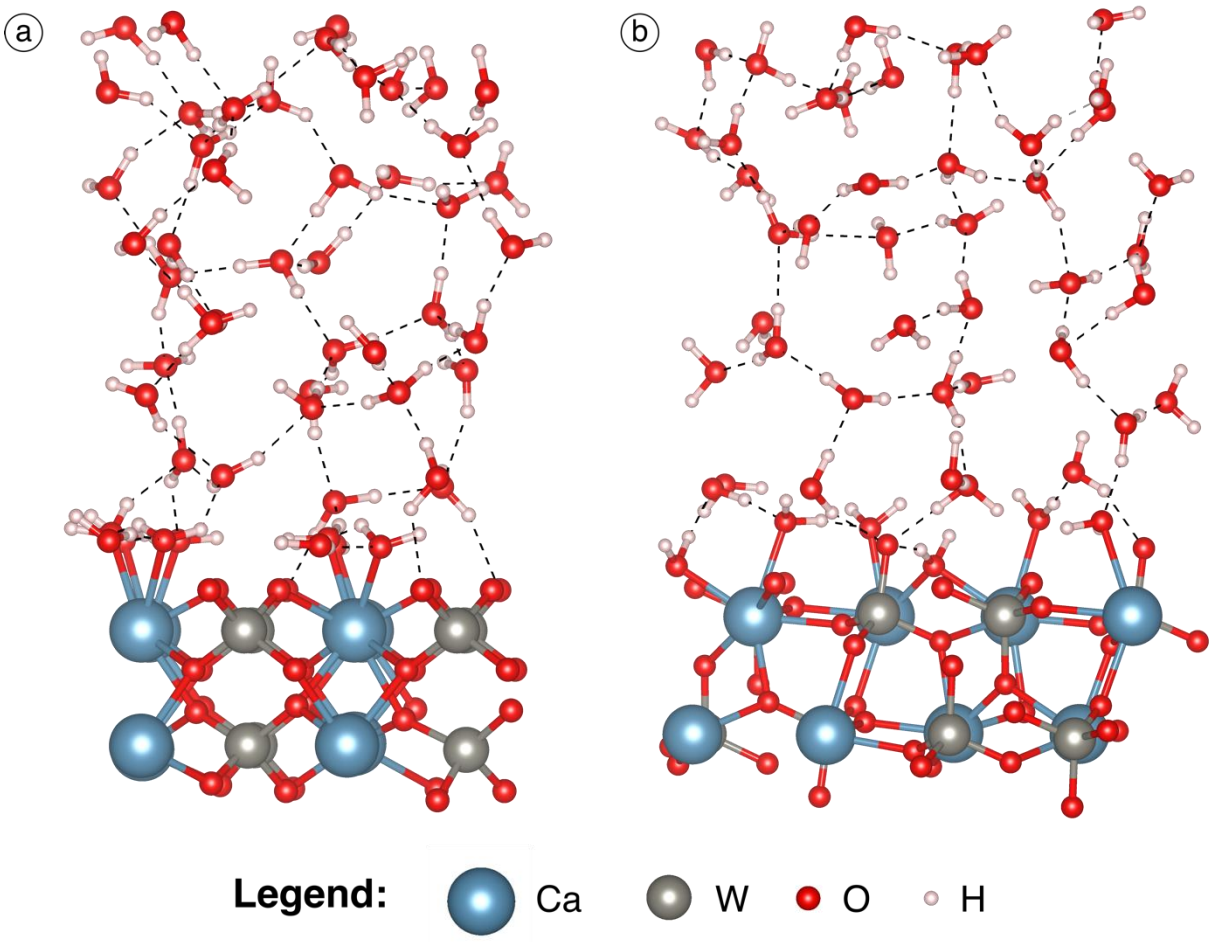



Figure 9. Snapshots of side views of the (001) (a) and (112) (b) scheelite surfaces above which the space has been completely filled with water molecules. Dashed lines represent hydrogen bonds. Lone atoms and repeated boundaries are due to the periodicity of the cell.

Then, for each surface, the cell was completely filled with water molecules to attain a density of 1.00 g $cm^{-3}$. Since the water molecules interact with the two reciprocal surfaces of the slabs, we did not use these simulations for adsorption energy computations but only to assess the behavior of scheelite surfaces in the presence of a full hydrated cell. Snapshots of the AIMD simulations are presented in Figure 9. For the (001) surface, the adsorption of two water molecules per calcium atom, observed previously, also occurs for the full hydrated cell (Figure 9a). Also, three water molecules are adsorbed by hydrogen bond established with oxygen atoms of surface tungstate anions. For the bulk of water, the geometries are structured

in such a way that the two H of two molecules point towards an oxygen of another molecule (Figure 9a). The H atoms of the two other molecules establish hydrogen bonds with other multi-molecular structures, forming clusters of water molecules intensively described and characterized in the literature, including by DFT [94–97]. Besides, the four calcium atoms of the (112) surface are occupied by six adsorbed water molecules (Figure 9b): four water molecules are adsorbed on the four surface calcium atoms while two additional molecules adsorb between two calcium atoms, as observed for a lower coverage (see Figure 5b) and for the monolayer (Figure 8b). Also, three water molecules adsorb by establishing hydrogen bonds with surface tungstate anions.

## Conclusions

In this work, the interplay between the (001) and the (112) surfaces of scheelite and water molecules has been investigated using adsorption experiments combined with *ab initio* molecular dynamics calculations. The results demonstrated that the adsorption of dissociated water is favorable on the two scheelite surfaces with, nonetheless, an exothermic adsorption only for the (112) surface. This indicates a significant ability of scheelite surfaces to be hydroxylated, which probably results in a low hydroxylation pH. Besides, since scheelite is a semi-soluble salt, the substitution of $WO_4^{2-}$ by $HO^-$ on the surface was investigated and was found to be energetically unfavorable for both surfaces. Overall, water adsorbs most favorably in its molecular form, on a single calcium atom in the case of the (001) surface and between two calcium atoms in the case of the (112) surface. The very first water molecules adsorb with $\Delta H_{ads} \approx$ -80 kJ·mol$^{-1}$ on (001) surface, and with $\Delta H_{ads} \approx$ -117 kJ·mol$^{-1}$ on (112) surface at 300 K, which is in very good agreement with the value of -90 kJ·mol$^{-1}$ calculated from the experimental data. For the latter, several adsorption models were tested to calculate the

isosteric enthalpy of adsorption, and we found that a dual-site Freundlich-Langmuir model fits the experimental data with excellent accuracy ($R^2$ = 0.9998). We therefore used those models to determine, by the Clausius-Clapeyron approach, the isosteric enthalpy of adsorption, which is in very good agreement with the theoretical values. In the experimental data, the two aforementioned surfaces are exposed and, therefore, the experimental isosteric enthalpy of adsorption is probably an average of the isosteric enthalpy of adsorption of each surface. Interestingly, when the monolayer is completed, each surface calcium atom on the (001) surface exhibits two adsorbed water molecules, while each surface calcium atom on the (112) surface displays one water molecule adsorbed with a water molecule adsorbed between two surface calcium atoms, resulting in three water molecules adsorbed on two calcium atoms. The isosteric enthalpies of adsorption of water on scheelite (-90 $kJ \cdot mol^{-1}$) are quite significant compared to those on fluorite (-55 $kJ \cdot mol^{-1}$) [56], which is the main problematic mineral in scheelite flotation. Therefore, desorption of water molecules from the surface, which is however required to subsequently adsorb the collector molecules [98], will need more energy for scheelite than for fluorite. This probably explains the lower flotation ability of scheelite compared to fluorite reported in the literature. Historically, this problem has been overcome by heating the flotation pulp to increase the scheelite floatability. This corresponds to the Petrov process, developed in 1940 and widely used since [25,99]. Considering our results, it is now clear that this heating allows erasing the differences of floatability between fluorite and scheelite by providing enough energy to the system to desorb water molecules from the scheelite surfaces. Besides, new collectors that do not require desorption of water molecules from the surface could be used to increase the flotation selectivity towards scheelite, *e.g.*, collectors that adsorb bridged on a water molecule adsorbed on the surface.

## Acknowledgments

This work was granted access to the HPC resources of TGCC under the allocation 2020-A0080910433 made by GENCI. This work was also performed using the HPC Mesocenter "Explor". The IJL members acknowledge FEDER funding trough TALiSMAN (LO0019535) project. We finally want to thank Prof. Lev Filippov for providing the scheelite sample.

## References

[1] W. Xu, H. Zhao, Y. Li, L. Zheng, Z. Zhang, W. Cao, Optical temperature sensing through the upconversion luminescence from Ho3+/Yb3+ codoped CaWO4, Sensors and Actuators B: Chemical. 188 (2013) 1096–1100. https://doi.org/10.1016/j.snb.2013.07.094.

[2] J.H. Ryu, S.Y. Bang, J.-W. Yoon, C.S. Lim, K.B. Shim, Pulsed laser induced synthesis of scheelite-type colloidal nanoparticles in liquid and the size distribution by nanoparticle tracking analysis, Applied Surface Science. 253 (2007) 8408–8414. https://doi.org/10.1016/j.apsusc.2007.04.010.

[3] A.B. Campos, A.Z. Simões, E. Longo, J.A. Varela, V.M. Longo, A.T. de Figueiredo, F.S. De Vicente, A.C. Hernandes, Mechanisms behind blue, green, and red photoluminescence emissions in CaWO4 and CaMoO4 powders, Appl. Phys. Lett. 91 (2007) 051923. https://doi.org/10.1063/1.2766856.

[4] W. Cho, M. Yashima, M. Kakihana, A. Kudo, T. Sakata, M. Yoshimura, Room- temperature preparation of the highly crystallized luminescent $CaWO_4$ film by an electrochemical method, Appl. Phys. Lett. 66 (1995) 1027–1029. https://doi.org/10.1063/1.113563.

[5] Cz. Koepke, A.J. Wojtowicz, A. Lempicki, Excited-state absorption in excimer-pumped CaWO4 crystals, Journal of Luminescence. 54 (1993) 345–355. https://doi.org/10.1016/0022-2313(93)90003-6.

[6] M.J. Treadaway, R.C. Powell, Luminescence of calcium tungstate crystals, The Journal of Chemical Physics. 61 (1974) 4003–4011. https://doi.org/10.1063/1.1681693.

[7] D.S. Kim, M. Ostromecki, I.E. Wachs, Surface structures of supported tungsten oxide catalysts under dehydrated conditions, Journal of Molecular Catalysis A: Chemical. 106 (1996) 93–102. https://doi.org/10.1016/1381-1169(95)00186-7.

[8] A. Moffat, Mass transfer effects in the olefin disproportionation reaction I. Promoter concentration and temperature effects for propylene on WO3-silica catalysts, Journal of Catalysis. 22 (1971) 379–388. https://doi.org/10.1016/0021-9517(71)90210-7.

[9] W. Gr/:unert, R. Feldhaus, K. Anders, E.S. Shpiro, Kh.M. Minachev, Reduction behavior and

metathesis activity of catalystsIII. The activation of catalysts, Journal of Catalysis. 120 (1989) 444–456. https://doi.org/10.1016/0021-9517(89)90284-4.

[10] Z. Zhang, W. Wang, D. Jiang, J. Xu, Synthesis of dumbbell-like Bi2WO6@CaWO4 composite photocatalyst and application in water treatment, Applied Surface Science. 292 (2014) 948–953. https://doi.org/10.1016/j.apsusc.2013.12.084.

[11] W. Xu, Y. Cui, Y. Hu, L. Zheng, Z. Zhang, W. Cao, Optical temperature sensing in Er3+-Yb3+ codoped CaWO4 and the laser induced heating effect on the luminescence intensity saturation, Journal of Alloys and Compounds. 726 (2017) 547–555. https://doi.org/10.1016/j.jallcom.2017.08.007.

[12] N. Faure, C. Borel, M. Couchaud, G. Basset, R. Templier, C. Wyon, Optical properties and laser performance of neodymium doped scheelites CaWO4 and NaGd(WO4)2, Appl. Phys. B. 63 (1996) 593–598. https://doi.org/10.1007/BF01830998.

[13] A.A. Kaminskii, H.J. Eichler, K. Ueda, N.V. Klassen, B.S. Redkin, L.E. Li, J. Findeisen, D. Jaque, J. García-Sole, J. Fernández, R. Balda, Properties of Nd^3+-doped and undoped tetragonal PbWO_4, NaY(WO_4)_2, CaWO_4, and undoped monoclinic ZnWO_4 and CdWO_4 as laser-active and stimulated Raman scattering-active crystals, Appl. Opt. 38 (1999) 4533. https://doi.org/10.1364/AO.38.004533.

[14] J.H. Ryu, G.S. Park, K.M. Kim, C.S. Lim, J.-W. Yoon, K.B. Shim, Synthesis of CaWO4 nanocolloidal suspension via pulsed laser ablation and its optical properties, Appl. Phys. A. 88 (2007) 731–736. https://doi.org/10.1007/s00339-007-4051-4.

[15] K. Tanaka, K. Fukui, K. Ohga, C.-K. Choo, CaWO4 thin films synthesized by pulsed laser deposition, Journal of Vacuum Science & Technology A: Vacuum, Surfaces, and Films. 20 (2002) 486–491. https://doi.org/10.1116/1.1450583.

[16] D.R. Shearer, L.E. Rowe, Temperature dependence of x-ray induced luminescence from medical x-ray screens: Temperature dependence of x-ray screen luminescence, Med. Phys. 14 (1987) 197–201. https://doi.org/10.1118/1.596070.

[17] A. Yariv, S.P.S. Porto, K. Nassau, Optical Maser Emission from Trivalent Praseodymium in Calcium Tungstate, Journal of Applied Physics. 33 (1962) 2519–2521. https://doi.org/10.1063/1.1729008.

[18] L.F. Johnson, G.D. Boyd, K. Nassau, R.R. Soden, Continuous Operation of a Solid-State Optical Maser, Phys. Rev. 126 (1962) 1406–1409. https://doi.org/10.1103/PhysRev.126.1406.

[19] L.F. Johnson, R.A. Thomas, Maser Oscillations at 0.9 and 1.35 Microns in CaW O 4 : Nd 3 +, Phys. Rev. 131 (1963) 2038–2040. https://doi.org/10.1103/PhysRev.131.2038.

[20] S. Xiong, D. Liang, H. Wu, W. Lin, J. Chen, B. Zhang, Preparation, characterization, tribological and lubrication performances of Eu doped CaWO4 nanoparticle as anti-wear additive in water-soluble fluid for steel strip during hot rolling, Applied Surface Science. 539 (2021) 148090. https://doi.org/10.1016/j.apsusc.2020.148090.

[21] A.B.T. Werner, W.D. Sinclair, E.B. Amey, International Strategic Mineral Issues Summary Report - Tungsten. U.S. Geological Survey Circular 930-O. Available online at: http://pubs.usgs.gov/pdf/circular/c930-o.html, (1998).

[22] H. Schubert, H. Baldauf, W. Kramer, J. Schoenherr, Further development of fluorite flotation from ores containing higher calcite contents with oleoylsarcosine as collector, International Journal of Mineral Processing. 30 (1990) 185–193. https://doi.org/10.1016/0301-7516(90)90014-P.

[23] P. Pitfield, T. Brown, G. Gunn, D. Rayner, Tungsten Profile. London: British Geological Survey. Available online at: https://www.bgs.ac.uk/downloads/start.cfm?id=1981, (2011).

[24] X. Yang, Beneficiation studies of tungsten ores – A review, Minerals Engineering. 125 (2018) 111–119. https://doi.org/10.1016/j.mineng.2018.06.001.

[25] Y. Foucaud, L. Filippov, I. Filippova, M. Badawi, The Challenge of Tungsten Skarn Processing by Froth Flotation: A Review, Front. Chem. 8 (2020) 230. https://doi.org/10.3389/fchem.2020.00230.

[26] U.S. Geological Survey, Mineral Commodity Summaries 2019. Technical report, United States Geological Survey, Reston, Virginia, USA., (2019).

[27] European Commission, Critical raw materials for the EU: Report of the Ad-hoc Working Group on defining critical raw materials., (2010).

[28] U.S. Department of the Interior, Final List of Critical Minerals 2018, (2018).

[29] L.O. Filippov, Y. Foucaud, I.V. Filippova, M. Badawi, New reagent formulations for selective flotation of scheelite from a skarn ore with complex calcium minerals gangue, Minerals Engineering. 123 (2018) 85–94. https://doi.org/10.1016/j.mineng.2018.05.001.

[30] Y. Foucaud, I.V. Filippova, L.O. Filippov, Investigation of the depressants involved in the selective flotation of scheelite from apatite, fluorite, and calcium silicates: Focus on the sodium silicate/sodium carbonate system, Powder Technology. 352 (2019) 501–512. https://doi.org/10.1016/j.powtec.2019.04.071.

[31] Yann. Foucaud, Q. Dehaine, Lev.O. Filippov, I.V. Filippova, Application of Falcon Centrifuge as a Cleaner Alternative for Complex Tungsten Ore Processing, Minerals. 9 (2019) 448. https://doi.org/10.3390/min9070448.

[32] Y. Foucaud, I. Filippova, Q. Dehaine, P. Hubert, L. Filippov, Integrated approach for the processing of a complex tungsten Skarn ore (Tabuaço, Portugal), Minerals Engineering. 143 (2019) 105896. https://doi.org/10.1016/j.mineng.2019.105896.

[33] Y. Hu, Z. Gao, W. Sun, X. Liu, Anisotropic surface energies and adsorption behaviors of scheelite crystal, Colloids and Surfaces A: Physicochemical and Engineering Aspects. 415 (2012) 439–448. https://doi.org/10.1016/j.colsurfa.2012.09.038.

[34] Z. Gao, Y. Hu, W. Sun, J.W. Drelich, Surface-Charge Anisotropy of Scheelite Crystals, Langmuir. 32 (2016) 6282–6288. https://doi.org/10.1021/acs.langmuir.6b01252.

[35] B. Wills, J. Finch, an O.M.C. Safari, Wills' Mineral Processing Technology, 8th Edition, 2015. https://www.safaribooksonline.com/complete/auth0oauth2/&state=/library/view//9780080970547/?ar (accessed November 15, 2020).

[36] M.R. Atademir, J.A. Kitchener, H.L. Shergold, The surface chemistry and flotation of scheelite, II. Flotation "collectors," International Journal of Mineral Processing. 8 (1981) 9–16.

https://doi.org/10.1016/0301-7516(81)90003-X.

[37] K.I. Marinakis, G.H. Kelsall, The surface chemical properties of scheelite (CaWO4) II. Collector adsorption and recovery of fine scheelite particles at the iso-octane/water interface, Colloids and Surfaces. 26 (1987) 243–255. https://doi.org/10.1016/0166-6622(87)80119-1.

[38] K.H. Rao, K.S.E. Forssberg, Mechanism of oleate interaction on salt-type minerals Part III. Adsorption, zeta potential and diffuse reflectance FT-IR studies of scheelite in the presence of sodium oleate, Colloids and Surfaces. 54 (1991) 161–187. https://doi.org/10.1016/0166-6622(91)80058-V.

[39] N. Kupka, M. Rudolph, Froth flotation of scheelite – A review, International Journal of Mining Science and Technology. 28 (2018) 373–384. https://doi.org/10.1016/j.ijmst.2017.12.001.

[40] L.J. Warren, Shear-flocculation of ultrafine scheelite in sodium oleate solutions, Journal of Colloid and Interface Science. 50 (1975) 307–318. https://doi.org/10.1016/0021-9797(75)90234-9.

[41] Y. Gao, Z. Gao, W. Sun, Z. Yin, J. Wang, Y. Hu, Adsorption of a novel reagent scheme on scheelite and calcite causing an effective flotation separation, Journal of Colloid and Interface Science. 512 (2018) 39–46. https://doi.org/10.1016/j.jcis.2017.10.045.

[42] W. Zhang, Z. Feng, Y. Yang, W. Sun, S. Pooley, J. Cao, Z. Gao, Bi-functional hydrogen and coordination bonding surfactant: A novel and promising collector for improving the separation of calcium minerals, Journal of Colloid and Interface Science. 585 (2021) 787–799. https://doi.org/10.1016/j.jcis.2020.10.059.

[43] R. Deng, Y. Huang, Y. Hu, J. Ku, W. Zuo, W. Yin, Study of reverse flotation of calcite from scheelite in acidic media, Applied Surface Science. 439 (2018) 139–147. https://doi.org/10.1016/j.apsusc.2017.12.231.

[44] L. Dong, F. Jiao, W. Qin, H. Zhu, W. Jia, New insights into the carboxymethyl cellulose adsorption on scheelite and calcite: adsorption mechanism, AFM imaging and adsorption model, Applied Surface Science. 463 (2019) 105–114. https://doi.org/10.1016/j.apsusc.2018.08.192.

[45] Y. Hu, Y. Huang, R. Deng, L. Ma, W. Yin, Improvement Effect of $FeSO_4 \cdot 7H_2O$ on Flotation Separation of Scheelite from Fluorite, ACS Omega. 4 (2019) 11364–11371. https://doi.org/10.1021/acsomega.9b00941.

[46] E. Albanese, C. Di Valentin, G. Pacchioni, $H_2O$ Adsorption on $WO_3$ and $WO_{3-x}$ (001) Surfaces, ACS Appl. Mater. Interfaces. 9 (2017) 23212–23221. https://doi.org/10.1021/acsami.7b06139.

[47] K. Anand, V. Fournée, G. Prévot, J. Ledieu, É. Gaudry, Nonwetting Behavior of Al–Co Quasicrystalline Approximants Owing to Their Unique Electronic Structures, ACS Appl. Mater. Interfaces. 12 (2020) 15793–15801. https://doi.org/10.1021/acsami.9b20653.

[48] J.C.C. Santos, F.R. Negreiros, L.S. Pedroza, G.M. Dalpian, P.B. Miranda, Interaction of Water with the Gypsum (010) Surface: Structure and Dynamics from Nonlinear Vibrational Spectroscopy and Ab Initio Molecular Dynamics, J. Am. Chem. Soc. 140 (2018) 17141–17152. https://doi.org/10.1021/jacs.8b09907.

[49] H. Zhang, Z. Xu, D. Chen, B. Hu, Q. Zhou, S. Chen, S. Li, W. Sun, C. Zhang, Adsorption mechanism of water molecules on hematite (1 0 4) surface and the hydration microstructure, Applied

Surface Science. 550 (2021) 149328. https://doi.org/10.1016/j.apsusc.2021.149328.

[50] J. Chen, F. Min, L. Liu, C. Liu, Mechanism research on surface hydration of kaolinite, insights from DFT and MD simulations, Applied Surface Science. 476 (2019) 6–15. https://doi.org/10.1016/j.apsusc.2019.01.081.

[51] H. Yi, F. Jia, Y. Zhao, W. Wang, S. Song, H. Li, C. Liu, Surface wettability of montmorillonite (0 0 1) surface as affected by surface charge and exchangeable cations: A molecular dynamic study, Applied Surface Science. 459 (2018) 148–154. https://doi.org/10.1016/j.apsusc.2018.07.216.

[52] J.M. Cases, F. Villieras, Thermodynamic model of ionic and nonionic surfactants adsorption-abstraction on heterogeneous surfaces, Langmuir. 8 (1992) 1251–1264. https://doi.org/10.1021/la00041a005.

[53] A. Nuhnen, C. Janiak, A practical guide to calculate the isosteric heat/enthalpy of adsorption *via* adsorption isotherms in metal–organic frameworks, MOFs, Dalton Trans. 49 (2020) 10295–10307. https://doi.org/10.1039/D0DT01784A.

[54] D. Farrusseng, C. Daniel, C. Gaudillère, U. Ravon, Y. Schuurman, C. Mirodatos, D. Dubbeldam, H. Frost, R.Q. Snurr, Heats of Adsorption for Seven Gases in Three Metal−Organic Frameworks: Systematic Comparison of Experiment and Simulation, Langmuir. 25 (2009) 7383–7388. https://doi.org/10.1021/la900283t.

[55] K. Sumida, D.L. Rogow, J.A. Mason, T.M. McDonald, E.D. Bloch, Z.R. Herm, T.-H. Bae, J.R. Long, Carbon Dioxide Capture in Metal–Organic Frameworks, Chem. Rev. 112 (2012) 724–781. https://doi.org/10.1021/cr2003272.

[56] Y. Foucaud, M. Badawi, L.O. Filippov, I.V. Filippova, S. Lebègue, Surface Properties of Fluorite in Presence of Water: An Atomistic Investigation, J. Phys. Chem. B. 122 (2018) 6829–6836. https://doi.org/10.1021/acs.jpcb.8b02717.

[57] R. Khatib, E.H.G. Backus, M. Bonn, M.-J. Perez-Haro, M.-P. Gaigeot, M. Sulpizi, Water orientation and hydrogen-bond structure at the fluorite/water interface, Sci Rep. 6 (2016) 24287. https://doi.org/10.1038/srep24287.

[58] N.H. de Leeuw, J.A. Purton, S.C. Parker, G.W. Watson, G. Kresse, Density functional theory calculations of adsorption of water at calcium oxide and calcium fluoride surfaces, Surface Science. 452 (2000) 9–19. https://doi.org/10.1016/S0039-6028(00)00288-0.

[59] N.H. de Leeuw, T.G. Cooper, A computational study of the surface structure and reactivity of calcium fluoride, J. Mater. Chem. 13 (2003) 93–101. https://doi.org/10.1039/b208004d.

[60] T.G. Cooper, N.H. de Leeuw, A combined ab initio and atomistic simulation study of the surface and interfacial structures and energies of hydrated scheelite: introducing a CaWO4 potential model, Surface Science. 531 (2003) 159–176. https://doi.org/10.1016/S0039-6028(03)00362-5.

[61] Y. Foucaud, M. Badawi, L. Filippov, I. Filippova, S. Lebègue, A review of atomistic simulation methods for surface physical-chemistry phenomena applied to froth flotation, Minerals Engineering. 143 (2019) 106020. https://doi.org/10.1016/j.mineng.2019.106020.

[62] J.D. Evans, G. Fraux, R. Gaillac, D. Kohen, F. Trousselet, J.-M. Vanson, F.-X. Coudert,

Computational Chemistry Methods for Nanoporous Materials, Chem. Mater. 29 (2017) 199–212. https://doi.org/10.1021/acs.chemmater.6b02994.

[63] Y. Foucaud, M. Badawi, L.O. Filippov, O. Barres, I.V. Filippova, S. Lebègue, Synergistic adsorptions of $Na_2CO_3$ and $Na_2SiO_3$ on calcium minerals revealed by spectroscopic and *ab initio* molecular dynamics studies, Chem. Sci. 10 (2019) 9928–9940. https://doi.org/10.1039/C9SC03366A.

[64] A. Geneyton, Y. Foucaud, L.O. Filippov, N.-E. Menad, A. Renard, M. Badawi, Synergistic adsorption of lanthanum ions and fatty acids for efficient rare-earth phosphate recovery: Surface analysis and ab initio molecular dynamics studies, Applied Surface Science. 526 (2020) 146725. https://doi.org/10.1016/j.apsusc.2020.146725.

[65] P. Liu, V. Johansson, H. Trilaksana, J. Rosdahl, G.G. Andersson, L. Kloo, EXAFS, ab Initio Molecular Dynamics, and NICIS Spectroscopy Studies on an Organic Dye Model at the Dye-Sensitized Solar Cell Photoelectrode Interface, ACS Appl. Mater. Interfaces. 9 (2017) 19773–19779. https://doi.org/10.1021/acsami.7b01779.

[66] J. Rouquerol, P. Llewellyn, F. Rouquerol, Is the bet equation applicable to microporous adsorbents?, in: P.L. Llewellyn, F. Rodriquez-Reinoso, J. Rouqerol, N. Seaton (Eds.), Studies in Surface Science and Catalysis, Elsevier, 2007: pp. 49–56. https://doi.org/10.1016/S0167-2991(07)80008-5.

[67] F. Rouquerol, J. Rouquerol, K. Sing, Adsorption by Powders and Porous Solids, Elsevier, 1999. https://doi.org/10.1016/B978-0-12-598920-6.X5000-3.

[68] D. Nicholson, T. Stubos, Simulation of Adsorption in Micropores, in: Membrane Science and Technology, Elsevier, 2000: pp. 231–256. https://doi.org/10.1016/S0927-5193(00)80011-X.

[69] S. Sircar, D.V. Cao, Heat of Adsorption, Chem. Eng. Technol. 25 (2002) 945–948. https://doi.org/10.1002/1521-4125(20021008)25:10<945::AID-CEAT945>3.0.CO;2-F.

[70] N. Ayawei, A.N. Ebelegi, D. Wankasi, Modelling and Interpretation of Adsorption Isotherms, Journal of Chemistry. 2017 (2017) 1–11. https://doi.org/10.1155/2017/3039817.

[71] I. Langmuir, THE ADSORPTION OF GASES ON PLANE SURFACES OF GLASS, MICA AND PLATINUM., J. Am. Chem. Soc. 40 (1918) 1361–1403. https://doi.org/10.1021/ja02242a004.

[72] J. Toth, State equation of the solid-gas interface layers, Acta Chim. Hung. 69 (1971) 311–328.

[73] R. Sips, On the Structure of a Catalyst Surface, The Journal of Chemical Physics. 16 (1948) 490–495. https://doi.org/10.1063/1.1746922.

[74] H. Freundlich, Über die Adsorption in Lösungen, Zeitschrift Für Physikalische Chemie. 57U (1907). https://doi.org/10.1515/zpch-1907-5723.

[75] K. LEVENBERG, A METHOD FOR THE SOLUTION OF CERTAIN NON-LINEAR PROBLEMS IN LEAST SQUARES, Quarterly of Applied Mathematics. 2 (1944) 164–168.

[76] D.W. Marquardt, An Algorithm for Least-Squares Estimation of Nonlinear Parameters, Journal of the Society for Industrial and Applied Mathematics. 11 (1963) 431–441.

[77] SciPy 1.0 Contributors, P. Virtanen, R. Gommers, T.E. Oliphant, M. Haberland, T. Reddy, D. Cournapeau, E. Burovski, P. Peterson, W. Weckesser, J. Bright, S.J. van der Walt, M. Brett, J. Wilson,

K.J. Millman, N. Mayorov, A.R.J. Nelson, E. Jones, R. Kern, E. Larson, C.J. Carey, İ. Polat, Y. Feng, E.W. Moore, J. VanderPlas, D. Laxalde, J. Perktold, R. Cimrman, I. Henriksen, E.A. Quintero, C.R. Harris, A.M. Archibald, A.H. Ribeiro, F. Pedregosa, P. van Mulbregt, SciPy 1.0: fundamental algorithms for scientific computing in Python, Nat Methods. 17 (2020) 261–272. https://doi.org/10.1038/s41592-019-0686-2.

[78] R.M. Hazen, L.W. Finger, J.W.E. Mariathasan, High-pressure crystal chemistry of scheelite-type tungstates and molybdates, Journal of Physics and Chemistry of Solids. 46 (1985) 253–263. https://doi.org/10.1016/0022-3697(85)90039-3.

[79] T.G. Cooper, N.H. de Leeuw, A Computer Modeling Study of the Competitive Adsorption of Water and Organic Surfactants at Surfaces of the Mineral Scheelite, Langmuir. 20 (2004) 3984–3994. https://doi.org/10.1021/la049796w.

[80] P. Mogilevsky, T.A. Parthasarathy, M.D. Petry, Anisotropy in room temperature microhardness and fracture of CaWo4 scheelite, Acta Materialia. 52 (2004) 5529–5537. https://doi.org/10.1016/j.actamat.2004.08.022.

[81] A. Neiman, Cooperative transport in oxides: Diffusion and migration processes involving Mo(VI), W(VI), V(V) and Nb(V), Solid State Ionics. 83 (1996) 263–273. https://doi.org/10.1016/0167-2738(95)00247-2.

[82] G. Kresse, J. Hafner, *Ab initio* molecular dynamics for liquid metals, Phys. Rev. B. 47 (1993) 558–561. https://doi.org/10.1103/PhysRevB.47.558.

[83] J.P. Perdew, K. Burke, M. Ernzerhof, Generalized Gradient Approximation Made Simple, Physical Review Letters. 77 (1996) 3865–3868. https://doi.org/10.1103/PhysRevLett.77.3865.

[84] P.E. Blöchl, Projector augmented-wave method, Phys. Rev. B. 50 (1994) 17953–17979. https://doi.org/10.1103/PhysRevB.50.17953.

[85] G. Kresse, D. Joubert, From ultrasoft pseudopotentials to the projector augmented-wave method, Phys. Rev. B. 59 (1999) 1758–1775. https://doi.org/10.1103/PhysRevB.59.1758.

[86] W. Kohn, L.J. Sham, Self-Consistent Equations Including Exchange and Correlation Effects, Phys. Rev. 140 (1965) A1133–A1138. https://doi.org/10.1103/PhysRev.140.A1133.

[87] G. Kresse, J. Furthmüller, Efficient iterative schemes for *ab initio* total-energy calculations using a plane-wave basis set, Phys. Rev. B. 54 (1996) 11169–11186. https://doi.org/10.1103/PhysRevB.54.11169.

[88] S. Grimme, Semiempirical GGA-type density functional constructed with a long-range dispersion correction, Journal of Computational Chemistry. 27 (2006) 1787–1799. https://doi.org/10.1002/jcc.20495.

[89] S. Nosé, A unified formulation of the constant temperature molecular dynamics methods, The Journal of Chemical Physics. 81 (1984) 511–519. https://doi.org/10.1063/1.447334.

[90] W.G. Hoover, Canonical dynamics: Equilibrium phase-space distributions, Physical Review A. 31 (1985) 1695–1697. https://doi.org/10.1103/PhysRevA.31.1695.

[91] M. Thommes, K. Kaneko, A.V. Neimark, J.P. Olivier, F. Rodriguez-Reinoso, J. Rouquerol, K.S.W. Sing, Physisorption of gases, with special reference to the evaluation of surface area and pore

size distribution (IUPAC Technical Report), Pure and Applied Chemistry. 87 (2015) 1051–1069. https://doi.org/10.1515/pac-2014-1117.

[92] P.A. Thiel, T.E. Madey, The interaction of water with solid surfaces: Fundamental aspects, Surface Science Reports. 7 (1987) 211–385. https://doi.org/10.1016/0167-5729(87)90001-X.

[93] A. Rahaman, V.H. Grassian, C.J. Margulis, Dynamics of Water Adsorption onto a Calcite Surface as a Function of Relative Humidity, J. Phys. Chem. C. 112 (2008) 2109–2115. https://doi.org/10.1021/jp077594d.

[94] T. Anacker, J. Friedrich, New accurate benchmark energies for large water clusters: DFT is better than expected, Journal of Computational Chemistry. 35 (2014) 634–643. https://doi.org/10.1002/jcc.23539.

[95] M.J. Gillan, D. Alfè, A. Michaelides, Perspective: How good is DFT for water?, The Journal of Chemical Physics. 144 (2016) 130901. https://doi.org/10.1063/1.4944633.

[96] S. Maheshwary, N. Patel, N. Sathyamurthy, A.D. Kulkarni, S.R. Gadre, Structure and Stability of Water Clusters $(H_2O)_n$, $n = 8-20$: An Ab Initio Investigation, The Journal of Physical Chemistry A. 105 (2001) 10525–10537. https://doi.org/10.1021/jp013141b.

[97] A. Møgelhøj, A.K. Kelkkanen, K.T. Wikfeldt, J. Schiøtz, J.J. Mortensen, L.G. Pettersson, B.I. Lundqvist, K.W. Jacobsen, A. Nilsson, J.K. Nørskov, Ab initio van der Waals interactions in simulations of water alter structure from mainly tetrahedral to high-density-like, The Journal of Physical Chemistry B. 115 (2011) 14149–14160.

[98] Y. Foucaud, J. Lainé, L.O. Filippov, O. Barrès, W.J. Kim, I.V. Filippova, M. Pastore, S. Lebègue, M. Badawi, Adsorption mechanisms of fatty acids on fluorite unraveled by infrared spectroscopy and first-principles calculations, Journal of Colloid and Interface Science. 583 (2021) 692–703. https://doi.org/10.1016/j.jcis.2020.09.062.

[99] I.S. Petrov, A new method for flotation of poor scheelite ores., n.d.